Computation & theory

Kröhnkite-type K$_2$Mn(SO$_4$)$_2$(H$_2$O)$_2$ double salt: synthesis, structure, and properties

João G. de Oliveira Neto[1], Rossano Lang[2,*] , Jéssica A. O. Rodrigues[1], Carlos E. O. Gutiérrez[3], Manuel A. R. Murillo[4], Francisco F. de Sousa[1,5], José G. Silva Filho[1], and Adenilson O. dos Santos[1]

[1] *Center for Social Sciences, Health, and Technology, Federal University of Maranhão - UFMA, Imperatriz, MA 65900-410, Brazil*

[2] *Institute of Science and Technology, Federal University of São Paulo - UNIFESP, São José dos Campos, SP 12231-280, Brazil*

[3] *National Laboratory of Nanotechnology, Center for Research in Advanced Materials - Cimav, 31136 Chihuahua, CHIH, Mexico*

[4] *Engineering and Technology Institute, Autonomous University of Ciudad Juárez - UACJ, 32310 Ciudad Juárez, CHIH, Mexico*

[5] *Institute of Exact and Natural Sciences, Federal University of Pará - UFPA, Belém, PA 66075-110, Brazil*

ABSTRACT

A comprehensive study of the K$_2$Mn(SO$_4$)$_2$(H$_2$O)$_2$ double salt crystal with a kröhnkite-type framework is presented. Structural, morphological, thermal, vibrational, and optical properties have been explored and discussed. Moreover, calculations based on the density-functional perturbation theory were performed to accurately analyze inter- and intra-molecular vibrational modes, presenting 111 optical phonon modes in the spectral region of 50–3650 cm^{-1}. The X-ray diffraction studies confirmed that the K$_2$Mn(SO$_4$)$_2$(H$_2$O)$_2$ system crystallizes in triclinic symmetry with $P\bar{1}$ (C_i^1) space group. In addition, the crystal was thermally stable from 300 K up to near 360 K and has an optical band gap of 5.78 eV, typical of insulating material. Nevertheless, when optically excited at 3.1 eV (at 400 nm), *i.e.*, resonantly with the $^6A_{1g}(S) \rightarrow {}^4A_{1g}(G), {}^4E_g(G)$ electronic transition of Mn^{2+} ion, a dual-emission was detected: green–yellow ($\approx$ 562 nm) and orange ($\approx$ 598 nm—more intense emission), both corresponding to $^4T_{1g}(G) \rightarrow {}^6A_{1g}(S)$ de-excitation. The dual behavior is due to the two different Mn^{2+} luminescent species occupying slightly distorted octahedral (orange emission) and tetrahedral (green–yellow emission) sites. From the optical spectrum and Tanabe-Sugano diagram, the crystal-field strength and the Racah interelectronic-repulsion parameters were also estimated. The findings suggest that changes in the Mn coordination number (four- and six-fold) and in the crystalline field, the latter either by adequate doping or by the growth of mixed crystals, could lead to a tuning of the wavelength of the emitted light (from green to deep red).

🦋 Springer

GRAPHICAL ABSTRACT

krönhkite
$K_2Mn(SO_4)_2(H_2O)_2$
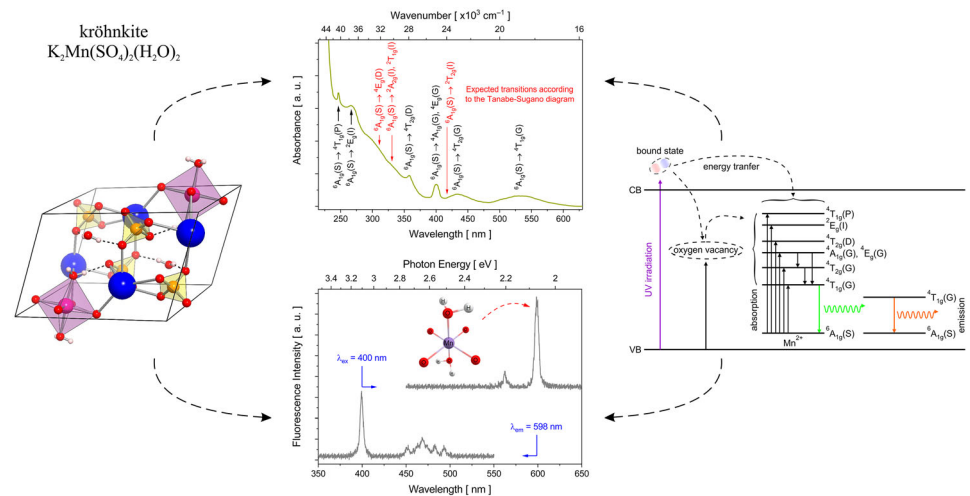
Introduction

Double salts dihydrates with a kröhnkite-type framework have attracted attention in several fields of science and technology due to their excellent structural stability and a large diversity of their properties, offering a wide range of possible applications. For instance, polyanions $(XO_4)^{n-}$-based materials have been explored as compounds for alkali-metal ion batteries [1–5].

This type of system has empirical formula A_n-$M(XO_4)_2(H_2O)_2$, where A is an alkaline metal ion, hydrogen cation, or ammonium ion (Na^+, K^+, Rb^+, Cs^+, H^+, NH_4^+, or Ca^{2+}), n is equal to 1 or 2, M is a metallic ion, such as Mg^{2+}, Mn^{2+}, Fe^{2+}, Co^{2+}, Ni^{2+}, Cu^{2+}, Zn^{2+}, Cd^{2+}, Al^{3+}, Fe^{3+}, In^{3+}, and Tl^{3+}. X is a site type that can be occupied by P^{5+}, As^{5+}, S^{6+}, Se^{6+}, Cr^{6+}, Mo^{6+}, and W^{6+} ions [6–10].

Although the literature has offered a range of experimental results of kröhnkite-type double salts [1–16], studies involving sulfate-based kröhnkite containing manganese and potassium are scarce. The $K_2Mn(SO_4)_2(H_2O)_2$ structure was firstly described by Fleck et al. [7]. According to the authors, the crystal structure is constituted by SO_4-tetrahedral and MnO_6-octahedral units. The structure has two H_2O

molecules at the corners of each octahedron; the other four atoms are bridging oxygens shared with $[SO_4]^{2-}$ ionic units. Furthermore, potassium atoms are connected to oxygens that link the tetrahedral-octahedral chains forming a three-dimensional kröhnkite-type structure.

To the best of our knowledge, there is no data available on the physical and chemical properties of $K_2Mn(SO_4)_2(H_2O)_2$. So here, a comprehensive study of the structural, morphological, thermal, vibrational, and optical properties of $K_2Mn(SO_4)_2(H_2O)_2$ crystal is proposed. However, this work is not only limited to the experimental reports. First-principle calculations based on the density-functional perturbation theory (DFPT) were performed to support the assignments of vibration modes observed through Fourier-transform infrared (FT-IR) and Raman spectroscopy. In addition, the crystal-field strength and the Racah interelectronic-repulsion parameters were evaluated from the optical spectrum and Tanabe-Sugano diagram.

By virtue of the inexpensive synthetic procedure and the possibility of color tunability by changes in the Mn coordination number and crystal-field strength, $K_2Mn(SO_4)_2(H_2O)_2$ arises as a promising material for optical applications. Divalent manganese cation (d^5 configuration) has been used as an efficient luminescent center in many host matrices [17–21].

Experimental details

Synthesis of K$_2$Mn(SO$_4$)$_2$(H$_2$O)$_2$ single crystals

K$_2$Mn(SO$_4$)$_2$(H$_2$O)$_2$ single crystals, labeled as K$_2$MnS$_2$H$_4$O$_{10}$, were grown by slow solvent evaporation from a saturated solution at a constant temperature (27 °C). For that, K$_2$SO$_4$ and MnSO$_4$(H$_2$O) (both from Sigma-Aldrich, purity > 99%) were used as starting materials in a 1:1 stoichiometric ratio (8.713 g:8.451 g, respectively). The precursor compounds were homogenized in 50 mL of deionized water using a magnetic stirrer (360 RPM) for 5 h, under a constant temperature of 323 K. The solution obtained was filtered to remove possible impurities and thereafter kept at 308 K for nucleation and crystal growth. Single crystals of light pink color with dimensions around 1.10 × 0.20 × 0.11 cm^3 (L × W × H) were harvested in 21 days. The crystals were removed from the solution by filtration, washed with acetone, and dried for 24 h at 308 K in atmospheric air.

Material characterizations

Powder X-ray diffraction pattern (PXRD) of powdered sample was acquired using a Panalytical Empyrean diffractometer operating at 40 kV/40 mA with Cu-Kα_1 (1.54056 Å) radiation. The measurement was performed at room temperature in the angular range of 2θ = 12–40° with steps of 0.02° and an acquisition time of 2 s. Rietveld refinement [22] using the GSAS/EXPGUI software [23, 24] was applied to the experimental pattern.

The surface morphology, microstructure, and elementary analysis were obtained by means of scanning electron microscopy (SEM) observations (JEOL JSM-7100F) coupled to an energy-dispersive X-ray spectroscopy analyzer (EDX). In addition, high-resolution transmission electron microscopy (HRTEM) images and electron diffraction of a selected area were acquired using a JEOL microscope (JEM 220FS-Cs model). SEM samples were prepared by directly spreading the powder over a carbon tape and coated with Au by sputtering. TEM samples were prepared in an ultrasonic ethanol dispersion, where a drop was used to deposit the material in a holey-carbon 200-mesh grid.

Thermogravimetry (TG) and differential thermal analysis (DTA) measurements were carried out in a simultaneous thermal analyzer Netzsch—STA 449 F3 Jupiter. In this synchronous thermoanalytical complex, the DTA data are converted into a heat flow (mW/mg) by an indirect measure since the sample and the reference share the same heat source. A fine powder sample weighing 19.78 mg was uniformly distributed on the platinum crucibles bottom (reference sample) and heated from 300 to 1253 K with a heating rate of 10 K/min under nitrogen atmosphere (50 mL/min).

FT-IR spectrum (average of 32 scans) of powdered sample mixed with KBr (KBr pellet method) was measured using a Bruker spectrophotometer (model Vertex 70 V). The data were recorded in the wavenumber range between 4000 and 400 cm^{-1}, with a spectral resolution of 4 cm^{-1}.

Raman spectroscopy was performed at ambient conditions using a Jobin–Yvon T64000 Raman spectrometer (three coupled 640 mm monochromators with 1800 grooves/mm holographic gratings) equipped with a charge-coupled device detection system. The sample was excited by the 514.5 nm line of a solid-state green laser. The average laser power on the sample surface was 2 mW using a 20 × lens, 0.25 aperture, and 26.5 focus. The Raman spectrum was recorded with an average of seven accumulations with 60 s time each, with a spectral resolution of 2 cm^{-1}.

Absorbance and transmittance spectra in the 200–700 nm wavelength region were assessed by an Evolution 220 UV–Vis-NIR spectrophotometer of dual-beam with a deuterium lamp from Thermo Scientific.

Fluorescence spectroscopy measurements in the emission and excitation regimes were performed by means of a Shimadzu spectrofluorometer (model RF-6000) using a Xe flash lamp as an excitation source. The emission spectrum was deconvolved using the color matching functions established by the Commission Internationale de l'Eclairage (CIE) 1931 for color spaces [25].

Computational calculations

The vibrational frequencies of the kröhnkite-type K$_2$Mn(SO$_4$)$_2$(H$_2$O)$_2$ structure were estimated via a dynamical matrix calculated by the DFPT [26, 27], implemented in the QUANTUM-ESPRESSO plane-wave code [28, 29]. For the exchange–correlation potential, the local spin density approximation

(LSDA) [29] was adopted, considering the Perdew-Zunger functional [30] with $4 \times 4 \times 4$ Monkhorst–Pack k-points [31] and a plane wave cut-off of 150 Ry. For the dispersion correction, the Grimme-D2 method was used [32]. The structure was fully relaxed (including the cell parameters) until the forces became smaller than 1×10^{-4} Ry/Bohr, stress less to 0.01 kbar, and an energy threshold = 1×10^{-12} Ry.

Results and discussion

PXRD and Rietveld refinement

The PXRD pattern of $K_2MnS_2H_4O_{10}$ crystal and corresponding refined pattern are shown in Fig. 1a. The cell parameters obtained are: $a = 6.575(4)$ Å, $b = 7.335(5)$ Å, $c = 10.698(6)$Å, $\alpha = 72.93(1)°$, $\beta = 73.95(3)°$, $\gamma = 69.72(4)°$, and $V = 453.44(9)$ Å^3, confirming that the double salt crystallizes in the triclinic symmetry, $P\bar{1}$ (C_i^1) space group with two formulas per unit cell ($Z = 2$). The final weighted (R_{wp}), R-factor profiles (R_p), and the goodness of fit indicator (S) were 12.4%, 8.8%, and 1.6, respectively. These values indicate that there is a good agreement between the literature data (ICSD-95862) [7] and the experimental pattern obtained herein.

A projection of the unit cell in polyhedral and ball-and-stick model are shown in Fig. 1b. The structure is formed by infinite $[Mn(SO_4)_2(H_2O)_2]^{2-}$ tetrahedral-octahedral chains, in which MnO_6 octahedral units are corner-linked to SO_4 tetrahedral ones by intermolecular interaction [8], as pictured in Fig. 1c. Moreover, hydrogen bonds are formed between the two independent H_2O molecules and SO_4 tetrahedrons, while the adjacent kröhnkite chains are connected to two distinct potassium atoms [7].

### SEM and EDX characterizations

Figure 2a depicts an SEM image of a $K_2MnS_2H_4O_{10}$ crystal as grown, in which its morphological characteristic in a polygonal-like shape can be noticed. Imperfections such as pores and cracks are also observable. Likely, the uncontrolled solvent evaporation rate directly influenced the structural order producing defects on the crystal surface during solid-phase growth.

Qualitative analysis by EDX spectroscopy on the crystal is shown in Fig. 2b. The elemental evaluation reveals the K, Mn, S, O, and C as sample constituents. The signal at 0.277 keV is attributed to the carbon from the carbon tape assembled in the sample holder.

HRTEM observations

Bright-field HRTEM observations of $K_2MnS_2H_4O_{10}$, the same used in the XRD analysis, were conducted in seeking a more meaningful understanding of when

Figure 1 **a** PXRD pattern at room temperature of $K_2MnS_2H_4O_{10}$ crystal, along with the corresponding Rietveld refinement analysis. **b** Salt unit cell in the triclinic phase along the *b*-axis showing the hydrogen bonds formed with H_2O molecules. **c** $2 \times 2 \times 2$ supercell parallel to the kröhnkite-type $[Mn(SO_4)_2(H_2O)_2]^{2-}$ chains.
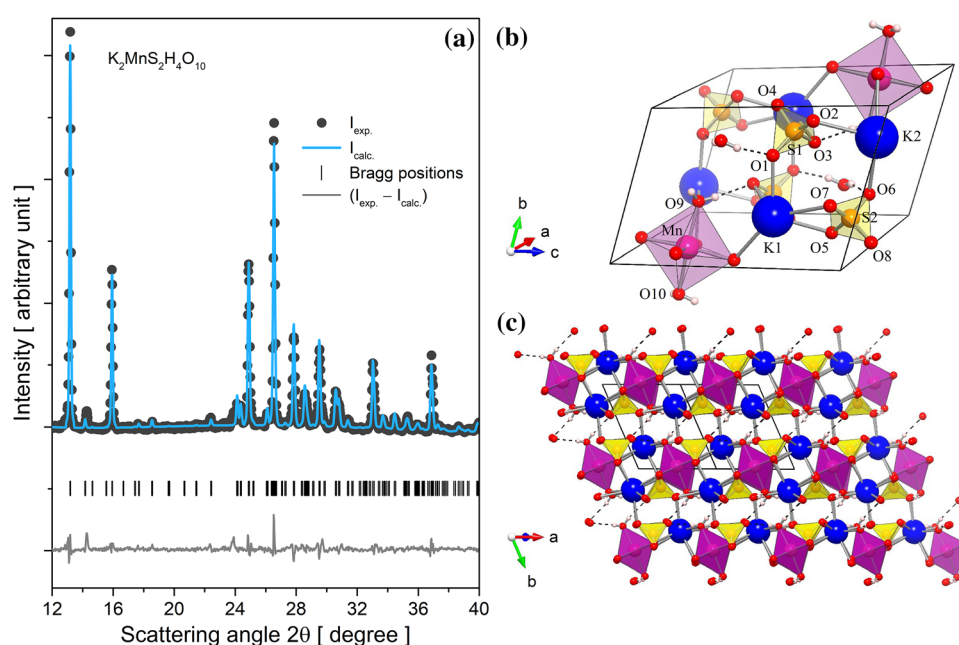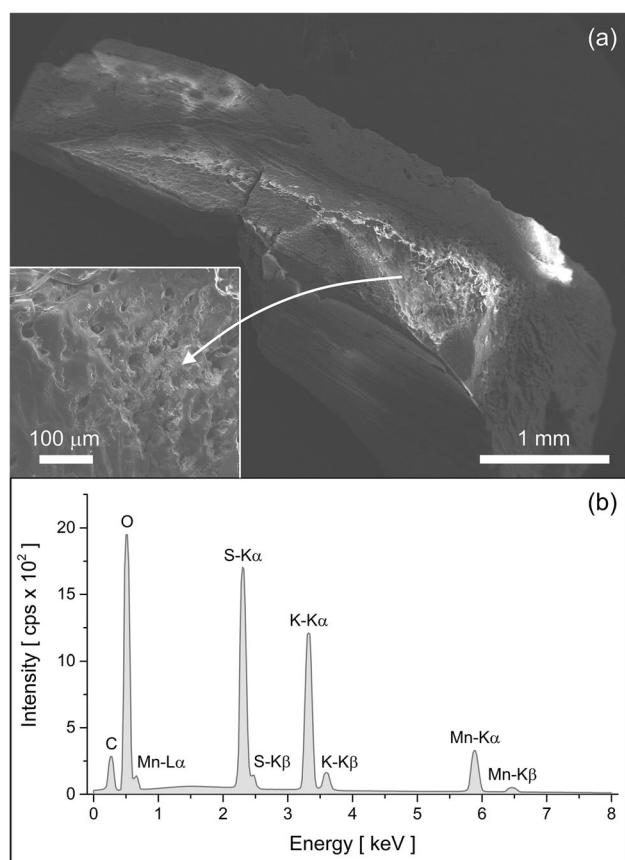
Figure 2 **a** SEM micrography, and **b** EDX elemental analysis spectrum of a $K_2MnS_2H_4O_{10}$ crystal.

the crystal is pulverized. As observed in Fig. 3a, the material in powdered form is characterized, as expected, by particles of irregular-shaped morphology. Herein, a particle (average diameter ranging of 0.3–1.8 μm) represents a grain agglomerate. It is important to know that the $K_2MnS_2H_4O_{10}$ crystal is extremely sensitive to electron beam radiation (Fig. 3b). After several attempts, a grain edge detail was obtained, as depicted in Fig. 3c. Electron diffraction of a selected area (Fig. 3d) corroborates the triclinic ordered atomic pattern, very similar to that reported for a triclinic phase of tricalcium silicate crystal [33].

Thermal (TG and DTA) analyses

TG–DTA coupled thermograms in the temperature range between 300 and 1253 K are shown in Fig. 4. In the TG curve, it is noticed that the $K_2MnS_2H_4O_{10}$ crystal is thermally stable from 300 K up to near 360 K. However, in the interval between 380 and 470 K, there are mass changes associated with the

dehydration of the double salt. The total mass loss corresponds to 8.39% (35.74 g/mol), equivalent to removing two metal-coordinated H_2O molecules. In the DTA curve between 300 and 470 K, it is possible to identify two endothermic peaks (Table 1). The peak (I) suggests a conformational phase change into the crystal lattice, since a mass variation does not accompany that event on the TG curve. The peak (II) confirms the complete dehydration of the crystal, implying a phase transformation from the dihydrate structure to the anhydrous phase. The dehydration process is always endothermal, and the contribution of the hydrogen bonding to the thermal effect is much less than that of M–O$_{water}$ type bonds. Moreover, the DTA curve shows a sharp decay above 470 K, suggesting a change in the specific heat with increasing temperature.

At higher temperatures (> 800 K), three more endothermic events are observed. The peak (III) seems to arise from a solid–solid transformation from K_2SO_4 in the $K_2Mn(SO_4)_2$ anhydrous phase, i.e., from the orthorhombic β-K_2SO_4 structure to the α-K_2SO_4 trigonal one. This thermal feature has been previously reported for salts involving K_2SO_4 as a constituent [34].

The remarkable endothermic peak IV is typical of a first-order phase transformation, and it can be attributed to the $MnSO_4$ melting, once its melting point occurs near 973 K [35]. On the other hand, the diffuse peak V comprises the start of mass loss and characterizes a decomposition of the K_2SO_4. A glassy residue was identified as a final product at about 1253 K and the percentages found are as high as 88.4%. Table 1 summarizes the thermal events observed in the DTA thermogram.

FT-IR spectroscopy

According to the site group analysis for $P\bar{1}$ space group (Schoenflies notation: C_i^1), the zone-center phonon modes have the following irreducible representation: $\Gamma = 57A_g + 57A_u$ (3n modes predicted by group theory, $n = 38$ = number of atoms in the primitive cell), where $3A_u$ are acoustic modes, and thus, remaining 111 optical modes represented by $\Gamma = 57A_g + 54A_u$. The modes belonging to the A_u irreducible representations are IR-active, whereas Raman activity is exhibited by those belonging to the A_g irreducible representations. To determine the calculated vibration modes of the $K_2MnS_2H_4O_{10}$

Figure 3 **a** TEM image in low magnification showing the morphology of $K_2MnS_2H_4O_{10}$ in the powdered form. **b** HRTEM of a crystalline grain showing electron beam sensitive damage as indicated by white arrows. **c** HRTEM near the edge of a grain. **d** Selected-area electron diffraction pattern indicating a triclinic phase.
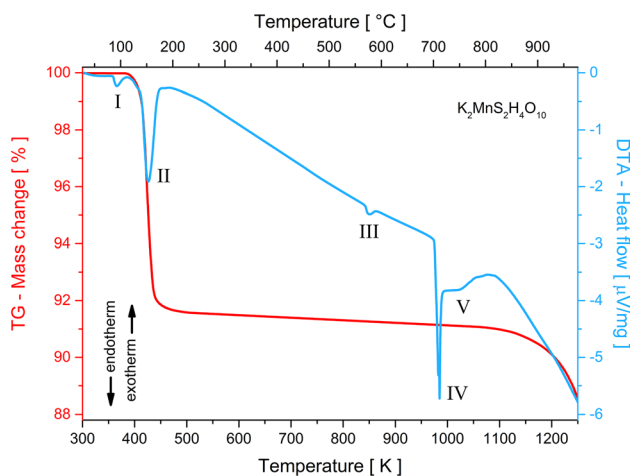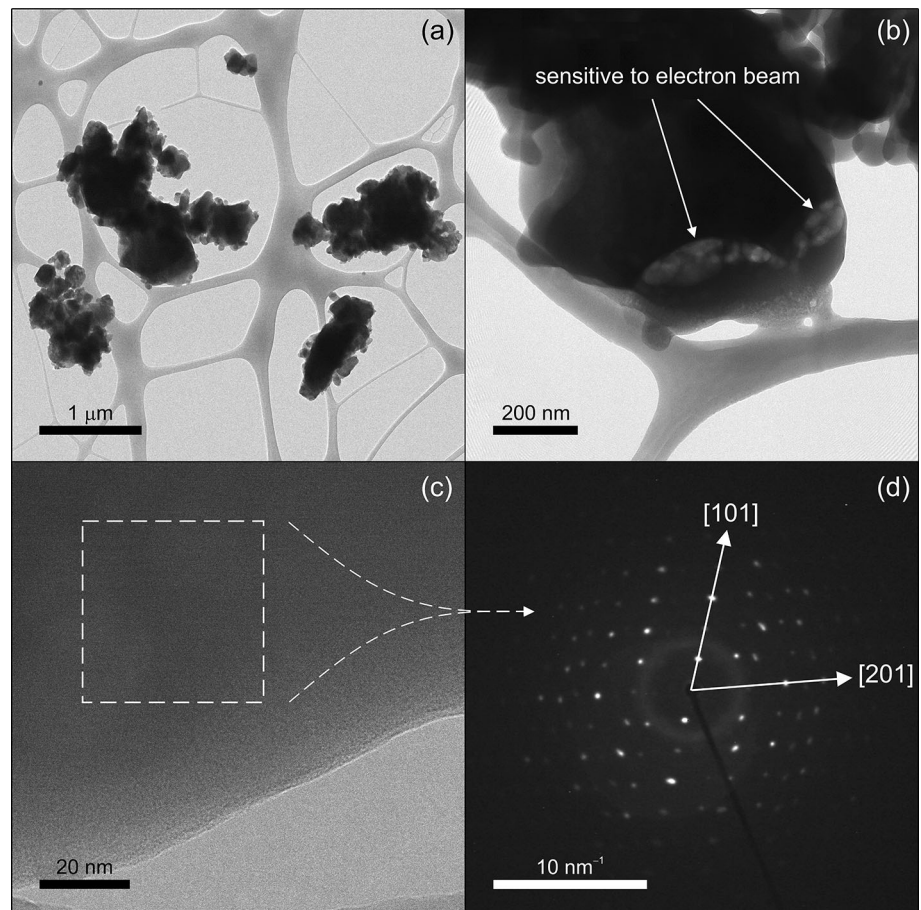

Figure 4 TG–DTA coupled thermograms of the $K_2MnS_2H_4O_{10}$ double salt dihydrate.

crystal, the crystal structure was duly optimized using the DFPT method from which the relaxed cell parameters were obtained. The optimized parameter values are compared with the experimental values reported in the literature [7], showing a good

agreement, as verified in Table S1 of supplementary material. The Raman and IR-active experimental modes and their corresponding assignments are given in Table 2. All the calculated vibration modes are provided in Table S2 (supplementary material).

Figure 5 shows the FT-IR experimental spectrum of powdered $K_2MnS_2H_4O_{10}$ crystal ranging from 400 to 4000 cm^{-1}, where the main bands are marked (insert, right). Two characteristic broadband of H_2O stretching vibrations is noticed between 3000 and 3600 cm^{-1}. In addition, some modes with vibrational contributions from the H_2O molecules, such as scissoring, twisting, wagging, and rocking are observed within the 400–1800 cm^{-1} range.

As suggested by crystal structure determination [7], several chemical bonds involve the H_2O molecules and $[SO_4]^{2-}$ groups in the kröhnkite framework, resulting in an extensive hydrogen bond system throughout the crystal lattice. The IR absorption bands centered at 1175, 1133, 1115, 1072, 617, and 469 cm^{-1} are duly described as contributions of vibrational features from $[SO_4]^{2-}$ tetrahedra linked to H_2O distorted structure.

Table 1 Endothermal events observed in the DTA thermogram for the $K_2MnS_2H_4O_{10}$ crystal when heated with a rate of 10 K/min

Peak	Event type	Assignment	Temperature (K)
I	Endo	Conformational change	365
II	Endo	Composition change ≡ dehydration	425
III	Endo	Transformation reaction	850
IV	Endo	Composition change ≡ melting	983
V	Endo	Start of decomposition	1055

Weak IR absorption bands corresponding to the τ(MnOSO) torsion modes have also been observed at around 439–449 cm^{-1}. Indeed, inorganic systems containing transition metals as coordination sphere centers have weak bands below 450 cm^{-1}, as reported by the literature [36].

Raman spectroscopy

Raman experimental spectra (non-polarized) in the 50–3650 cm^{-1} range are shown in Fig. 6. There are eight Raman bands in the wavenumber region below 200 cm^{-1} (Fig. 6a). These bands are associated with lattice vibration modes (intermolecular modes). According to our calculations (Table 2), the bands between 67 and 161 cm^{-1} have contribution from translational motions of K atoms combined with torsions/translations of MnO_6 and $[SO_4]^{2-}$ units. Additionally, vibration modes owing to a combination of bending, anti-symmetrical and symmetrical stretching involving the octahedral metal center appeared at around 179 and 197 cm^{-1}. Above 200 cm^{-1}, Raman-active modes identified nearly 216, 252, and 317 cm^{-1} are assigned as $v_a(MnO_6) + \delta(O2\cdot\cdot HO9H\cdot\cdot O5)$, sc(O9MnO7) + $\delta(O2\cdot\cdot HO9H\cdot\cdot O5)$, and $v(MnO9) + \delta(O2\cdot\cdot HO9H\cdot\cdot O5)$ motions, respectively.

Figure 6b illustrates the spectral region between 350 and 1250 cm^{-1}, in which there is a coupling of vibration modes belonging to $[SO_4]^{2-}$ tetrahedron units and H_2O motions. However, MnO_6 octahedron torsion vibrations appear as combined motions from tetrahedron units and H_2O molecules, mainly observed at about 441 and 468 cm^{-1}. The Raman modes near 618, 821, 880, 991, 1027, 1046, 1100, 1125, and 1167 cm^{-1} are ascribed as motions from molecular deformations in- and out-of-plane (rocking, wagging, scissoring, twisting, symmetric and anti-symmetric stretching) of $[SO_4]^{2-}$ and H_2O.

The highest wavenumber range between 2550 and 3650 cm^{-1} is shown in Fig. 6c. In this spectral region, a very broadband at around 3400 cm^{-1} has appeared: a fingerprint of anti-symmetric and symmetric stretching modes from the H_2O molecules.

Optical measurements

UV–Vis optical absorbance spectrum at room temperature of a $K_2MnS_2H_4O_{10}$ single crystal is shown in Fig. 7a. In the $[MnO_6]$ metal complex co-coordinated with four oxygen and two H_2O molecules, manganese has an oxidation state of 2 +, and the H_2O is a weak ligand. Six typical ligand-field bands of Mn^{2+} ions are then detected, supposedly arising from intraconfigurational transitions in octahedral coordination [37]. In the case of d^5-configuration, all transitions are doubly forbidden because they are spin-forbidden as $\Delta S \neq 0$ (there is only one electronic state with sextet spin multiplicity: the $^6A_{1g}(S)$ ground state), and orbitally (Laporte) forbidden as $\Delta L \neq +$ 1. Due to spin–orbit interactions, such transitions are not totally absent in the spectrum; however, they emerge with very weak intensity. The band positions and the respective assignments following the Tanabe-Sugano (T-S) energy-level diagram for the d^5-configuration [38–40], resulting in $\Delta_0/B = 12.5$ (see Fig. S1 in supplementary material), are given in Table 3.

It is likely that the cationic Mn ions into the kröhnkite framework mainly occupy sites of slightly lower symmetry (since it is clear for any site of $P\bar{1}$ space group), such as a C_{2v}, when compared to that highly regular O_h symmetry (perfect octahedral environment), for instance. There must be some distortion component in the octahedral crystal field surrounding the Mn^{2+}. Such a structural distortion can be associated with displacements of the oxygen atoms from the regular sites altering the Mn–O bond lengths [41]. Dangling bonds or even O^{2-} vacancies on the sixfold coordination also introduce strong structural disorders. If there is any symmetry distortion, the crystal field splitting will be affected.

The fundamental absorption property, which corresponds to electron excitation from the valance band

Table 2 Vibration mode analyses for the $K_2MnS_2H_4O_{10}$ crystal: calculated wavenumbers (ωcal), experimental Raman modes (ωR), experimental IR modes (ωIR), irreducible representation (Irrep.), and their assignments

ωcal (cm^{-1})	ωR (cm^{-1})	ωIR (cm^{-1})	Irrep	Assignments[*]
66.1	67	–	Ag	trans$_{op}$(S1O4 + S2O4) + trans$_{op}$(K1 + K2)
86.4	80	–	Ag	trans(MnO$_6$) + τ(MnO7S2O5) + τ(MnO3S1O2) + trans(K2)
94.9	95	–	Ag	ρ(S2O6O5) + ρ(S1O1O2) + δ(MnO$_6$) + trans(K1)
122.0	121	–	Ag	τ(MnO7S2O5) + τ(MnO3S1O2) + trans$_{op}$(K1 + K2)
133.4	136	–	Ag	τ(MnO7S2O5) + τ(MnO3S1O2) + trans(K2)
159.0	161	–	Ag	τ(MnO7S2O5) + τ(MnO3S1O2) + trans$_{op}$(K1 + K2)
182.3	179	–	Ag	va(MnO$_6$) + δ(MnO9O10) + vs(MnO7O4) + trans$_{ip}$ (K1 + K2)
198.9	197	–	Ag	va(MnO$_6$) + τ(MnO7S2O5) + τ(MnO3S1O2) + trans$_{ip}$ (K1 + K2)
211.9	216	–	Ag	va(MnO$_6$) + δ(O2··HO9H··O5)
238.4	252	–	Ag	sc(O9MnO7) + δ(O2··HO9H··O5)
324.7	317	–	Ag	v(MnO9) + δ(O2··HO9H··O5)
377.0	–	–	Ag	v(MnO10) + δ(O6··HO10H··O1) + ϕ(MnO3O4O7)
434.2	–	439	Au	sc(S1O1O2) + sc(S2O5O6) + τ(MnO3S2O4) + τ(MnO7S2O8)
448.0	441	–	Ag	tw(S1O1O2) + tw(S2O5O6) + τ(MnO3S2O4) + τ(MnO7S2O8) + ρ(O9H$_2$)
453.2	–	449	Au	tw(S1O1O2) + tw(S2O5O6) + τ(MnO3S2O4) + τ(MnO7S2O8) + ρ(O9H$_2$)
454.9	468	–	Ag	tw(S1O1O2) + tw(S2O5O6) + τ(MnO3S2O4) + τ(MnO7S2O8) + wag(O10H$_2$)
467.2	–	469	Au	sc(S1O1O3) + sc(S2O7O6) + wag(O10H$_2$)
555.3	–	545	Au	ρ(O10H$_2$) + wag(O9H$_2$)
599.5	–	603	Au	sc(S1O1O3) + sc(S2O5O8)
604.6	–	617	Au	ρ(O9H$_2$) + ρ(O10H$_2$) + wag(S1O1O3) + sc(S2O6O8)
609.9	618	–	Ag	ρ(O10H$_2$) + wag(S1O1O3) + sc(S2O7O8)
632.6	–	632	Au	ρ(O10H$_2$)
829.3	821	–	Ag	wag(O9H$_2$) + sc(O10H$_2$)
831.0	–	830	Au	wag(O9H$_2$) + sc(O10H$_2$)
897.8	880	–	Ag	wag(O9H$_2$) + sc(O10H$_2$)
901.9	–	883	Au	wag(O9H$_2$) + wag(O10H$_2$)
964.9	–	987	Au	wag(O9H$_2$) + tw(O10H$_2$)
972.0	991	–	Ag	wag(O9H$_2$) + tw(O10H$_2$)
1015.3	1027	–	Ag	va(S1O1O3) + va(S2O5O8) + ρ(O10H$_2$)
1043.9	1046	–	Ag	vs(S1O1O3) + vs(S1O2O4) + vs(S2O6O7) + ρ(O10H$_2$)
1071.0	–	1072	Au	vs(S1O1O3) + vs(S1O2O4) + vs(S2O5O8) + vs(S2O6O7) + ρ(O10H$_2$)
1099.8	1100	–	Ag	vs(S1O1O3) + vs(S1O2O4) + vs(S2O5O8) + vs(S2O6O7)
1103.0	–	1115	Au	va(S1O1O3) + va(S1O2O4) + va(S2O5O8) + va(S2O6O7) + tw(O9H$_2$) + wag(O10H$_2$)
1112.0	1125	–	Ag	va(S1O1O3) + va(S1O2O4) + tw(O9H$_2$) + tw(O10H$_2$)
1138.4	–	1133	Au	va(S1O1O3) + va(S1O2O4) + va(S2O5O8) + va(S2O6O7) + vs(O9H$_2$) + tw(O10H$_2$)
1142.1	–	1175	Ag	va(S1O2O4) + va(O9H$_2$)
1147.5	1167	–	Au	va(S1O1O3) + va(S1O2O4) + va(S2O5O8) + va(S2O6O7) + tw(O9H$_2$)
1545.0	–	1517	Au	sc(O9H$_2$) + sc(O10H$_2$)
1589.1	–	1639	Au	sc(O9H$_2$) + sc(O10H$_2$)
3230.0	–	3216	Au	vs(O9H$_2$) + vs(O10H$_2$)
3434.8	3408	–	Ag	va(O9H$_2$) + vs(O10H$_2$)
3496.9	–	3440	Au	va(O10H$_2$)

[*]Nomenclature: trans = translational; trans$_{ip}$ = translational in-phase; trans$_{op}$ = translational out-of-phase; τ = torsion; sc = scissoring; tw = twisting; ϕ = out-of-plane; wag = wagging; v = stretching; ρ = rocking; δ = bending; va = anti-symmetric stretching; vs = symmetric stretching

Figure 5 FT-IR spectrum of the $K_2MnS_2H_4O_{10}$ double salt dihydrate in the $400–4000$ cm^{-1} wavenumber range.

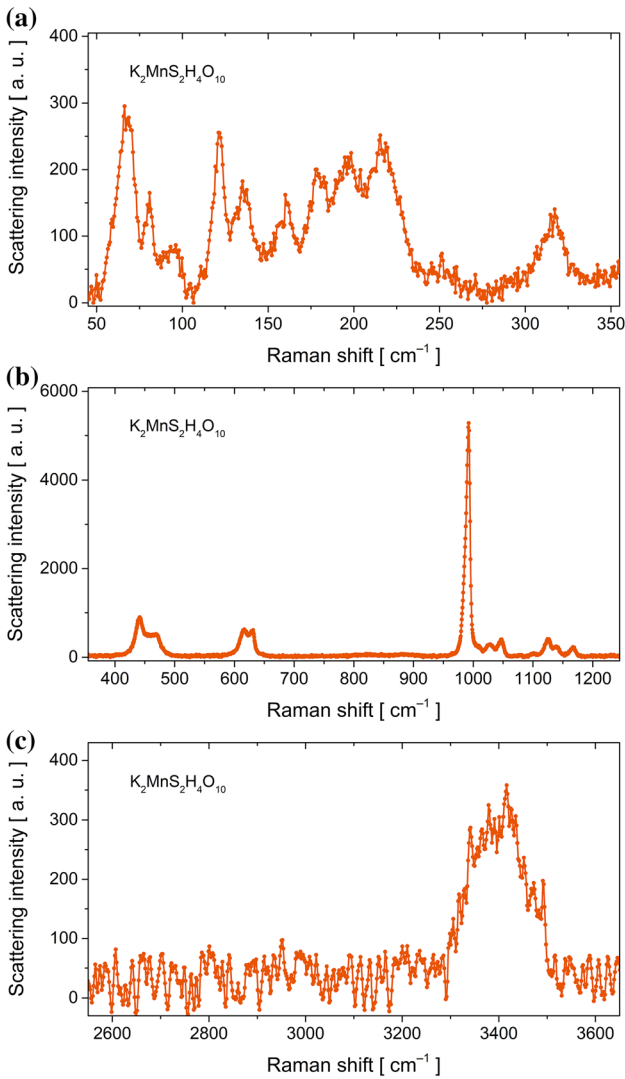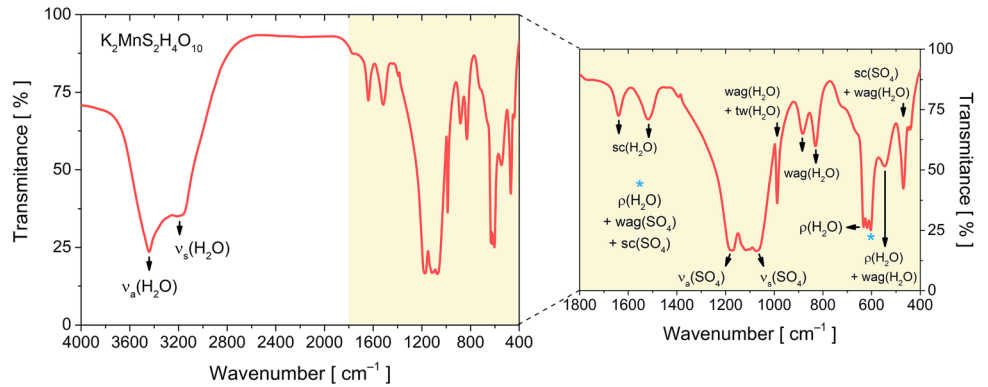**Figure 6** Raman experimental spectra of powdered $K_2MnS_2H_4O_{10}$ crystal in the wavenumber ranges: **a** $50–350$ cm^{-1}, **b** $350–1250$ cm^{-1}, and **c** $2550–3650$ cm^{-1}.
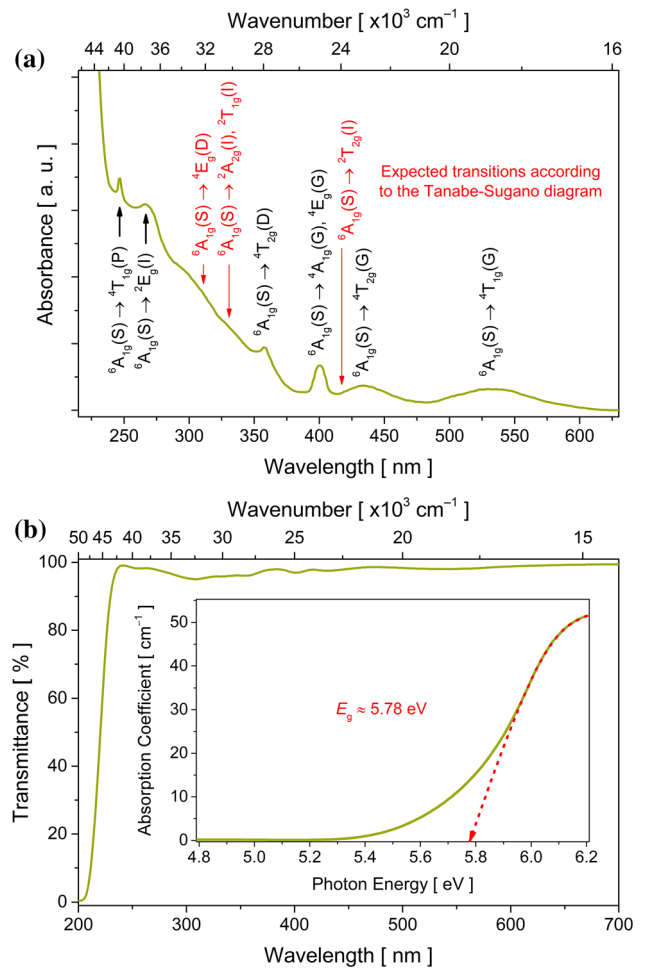

Figure 7 a UV–Vis optical absorbance spectrum of a $K_2MnS_2H_4O_{10}$ single crystal. **b** Transmittance spectrum and absorption coefficient assessed by Eq. (1).

Table 3 Experimental data obtained from the optical absorbance spectrum of Mn^{2+} ions into $K_2MnS_2H_4O_{10}$ crystal and into $MnSH_2O_5$ solubilized in deionized water.

Photoabsorption $^6A_{1g}(S) \rightarrow$	Wavelength (nm)		Wavenumber (cm^{-1})	
	$K_2MnS_2H_4O_{10}$	$MnSH_2O_5 + dw^*$	$K_2MnS_2H_4O_{10}$	$MnSH_2O_5 + dw^*$
$^4T_{1g}(P)$	246.5	–	40,567.9	–
$^2E_g(I)$	266.4	–	37,537.5	–
$^4E_g(D)$	–	–	–	–
$^2A_{2g}(I)$, $^2T_{1g}(I)$—degenerate	–	–	–	–
$^4T_{2g}(D)$	357.9	354.7	27,940.7	28,192.8
$^4A_{1g}(G)$, $^4E_g(G)$—degenerate	400.4	400.4	24,975.0	24,975.0
$^2T_{2g}(I)$	–	–	–	–
$^4T_{2g}(G)$	434.5	437.5	23,014.9	22,857.1
$^4T_{1g}(G)$	533.2	524.3	18,754.7	19,073.0

For the electronic transition assignments, the T–S diagram for d^5 configuration was used (Fig. S1)

*dw = deionized water

to conduction band, and the absorption coefficient (α), which describes the intensity attenuation of the light passing through crystal, were both evaluated by optical transmittance (T) as a function of wavelength (λ). The absorption coefficient was deduced using the following approximate relation:

$$\alpha(\lambda) = \frac{1}{d} \ln\left[\frac{(1 - R(\lambda))^2}{T(\lambda)}\right] \qquad (1)$$

where d is thickness, and R is the reflectance of the sample. As in the experiments, the reflectance signal was extremely low, thus $R = 0$ was assumed. The result is depicted in Fig. 7b inset. This rough estimation has been shown acceptable. It was also applied $\alpha(\lambda) = 2.303$ A(λ)/d, where A(λ) is the absorptance, which has converged to the same outcome. By extrapolating the straight portion of the data on abscissa at $\alpha(\lambda) = 0$, the optical bandgap was found near 5.78 eV. Such a high bandgap value is typical of insulating materials and associated with the bulk nature of the crystal.

In Fig. 8a, fluorescence spectra in the emission and excitation regimes are plotted. The photoemission spectrum was excited at 400 nm, *i.e.*, resonantly with the $^6A_{1g}(S) \rightarrow {}^4A_{1g}(G)$, $^4E_g(G)$ degenerate state. The energy of this transition hardly changes between $0 < \Delta_0/B < 28$ (see Fig. S1). With such optical excitation, surprisingly green-yellow (≈ 562 nm) and orange (≈ 598 nm—more intense) emissions are observed, both corresponding to $^4T_{1g}(G) \rightarrow {}^6A_{1g}(S)$ transition of the Mn^{2+} emissive center.

Generally, Mn^{2+} ion exhibits a broad emission peak, whose energy position depends on the coordination number and on the crystal-field strength from the local lattice. This way, the emission color (wavelength), attributed to $^4T_{1g}(G) \rightarrow {}^6A_{1g}(S)$ transition can be tuned from green to deep red. However, there was a dual-emission of the crystal with a sizable difference in intensity, indicating the contribution of different fluorescent centers in the radiative process. It is believed that individual Mn ions dominate the optical spectrum because there is a large distance between adjacent Mn into host units.

The emission band usually arises in the green-yellow spectral region for Mn^{2+} ions located in a tetrahedral arrangement (fourfold in T_d field, or slightly distorted). On the other hand, an octahedral environment (sixfold in O_h field, or slightly distorted) supports emissions in the orange-red region [42–45]. It is known that the crystal-field strength on octahedral geometry is much stronger than that of the tetrahedral one. As a result, larger splitting energy of the excited state in orbitals, and a lower energy of Mn^{2+} emission in the octahedral field can be noticed, corroborating the findings. Therefore, here, different fractions of Mn tetrahedrally coordinated, [MnO_4], and octahedrally coordinated, [MnO_6], supposedly contribute to the spectrum [46, 47]. Although such fractions in the $MnSO_4(H_2O)$ precursor compound are unknown and are not supplied by the manufacturer, the coexistence of two distinct luminescent
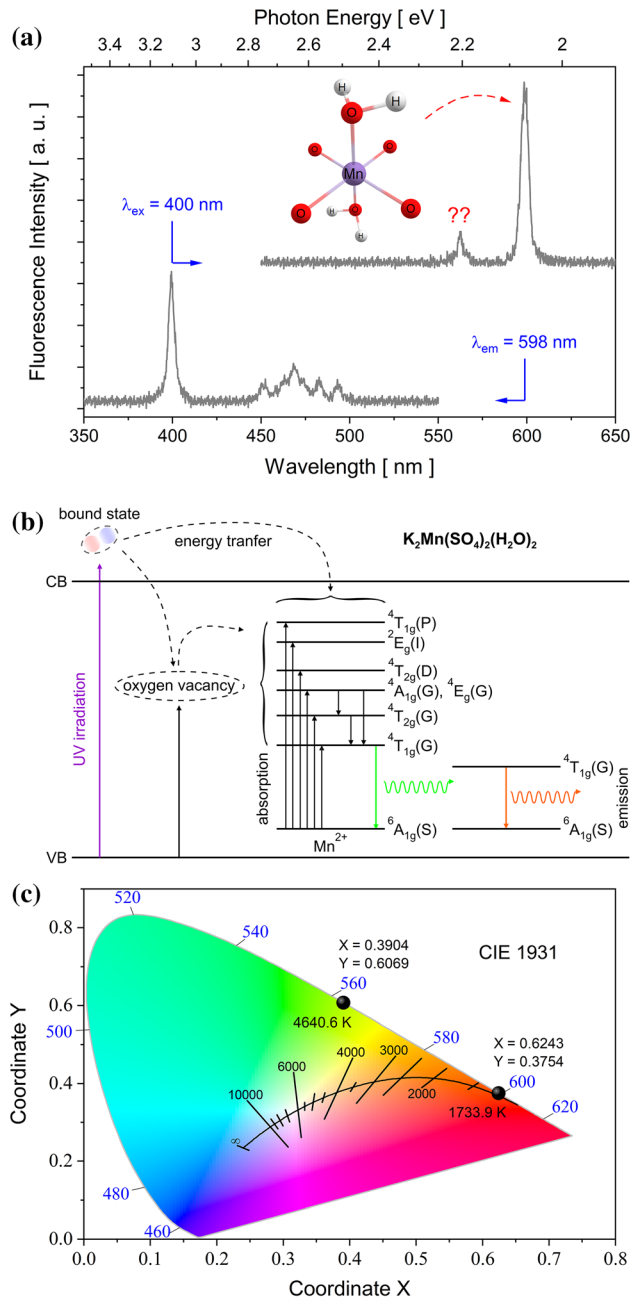
Figure 8 a Fluorescence spectra in the emission and excitation regimes. **b** Schematic illustration of possible excitation and de-excitation mechanisms and charge transfer processes for Mn^{2+} d-electron states **c** CIE chromaticity coordinates and CCT for green–ssyellow and orange emissions. The Planckian locus representing an incandescent blackbody radiator at various temperatures is also shown on the diagram for comparison.

species in the crystal structure explains why the complex possesses dual-emissive behavior.

The excitation spectrum, shown in Fig. 8a, was evaluated by monitoring the most intense emission at

598 nm. As can be noticed, different absorbing centers configure the spectrum. A characteristic relatively sharp peak centered at 399 nm corresponding to the $^6A_{1g}(S) \rightarrow {}^4A_{1g}(G)$, $^4E_g(G)$ electronic state, and a broadband structure (450–500 nm) with multiple peaks involve ligand-to-metal or defect-to-metal charge transfer, since such broadband does not comprise the energy bands of the $^6A_{1g}(S) \rightarrow {}^4T_{2g}(G)$ and $^6A_{1g}(S) \rightarrow {}^4T_{1g}(G)$ states observed in Fig. 7a.

Possible mechanisms for the excitation of the Mn^{2+} d-electron states are suggested in Fig. 8b. First, one must understand the chemical environment of Mn in the monohydrate sulfate lattice. Any light emission is promoted through efficient energy transfer from the host environment to Mn^{2+} ions, mediated by mixed electronic states. When Mn^{2+} ion is incorporated in the SO$_4$(H$_2$O) matrix, the cationic unoccupied centers are filled. Mixing between s-p electrons of the matrix and the d electrons of the Mn^{2+} ion occurs, and the transitions are partially allowed by the Laporte rule. This way, the [MnO$_4$(H$_2$O)$_2$]$^{6-}$ octahedral or [MnO$_4$]$^{6-}$ tetrahedral units act as absorbent luminescence centers, *i.e.*, they participate as exciton acceptors and further as emission centers that afford the $^4T_{1g}(G) \rightarrow {}^6A_{1g}(S)$ fluorescence.

In one mechanism, the exciton recombination at the Mn^{2+} sites can take it into excited states. The whole crystal lattice works as a UV light absorber and an exciton donor. However, the energy barrier for exciton transfer from K$^+$ and/or [SO$_4$]$^{2-}$ to [MnO$_4$(H$_{2-}$O)$_2$]$^{6-}$—[MnO$_4$]$^{6-}$ units should be investigated. Hybridization calculations involving K, S, O, and Mn orbitals to confirm possible coupling can address this issue. Another way encompasses photoexcited electrons in the crystal conduction band that may hop to O^{2-} vacancies and then jump to some Mn electronic state. In this case, the energy states related to oxygen defects must be greater than the Mn level. Ultimately, effective energy transfer processes by nonradiative intersystem crossing must also increase the exciton density in $^4T_{1g}(G)$, enhancing the fluorescence.

Using the corresponding CIE chromaticity (x, y) coordinates, it was possible to estimate the correlated color temperature (CCT) of the crystal employing McCamy's approximation algorithm [48]:

$$CCT = -449n^3 + 3525n^2 - 6823.3n + 5520.33 \qquad (2)$$

where, $n = (x–0.3320)/(y–0.1858)$. Substituting $(x, y) = (0.3904, 0.6069)$ for green–yellow and $(0.6243, 0.3754)$ for orange resultant emission, the CCT values were 4640.6 and 1733.9 K, respectively. The CIE color

coordinate diagram is illustrated in Fig. 8c. The Planckian locus was used as a reference illuminant for a comparison proposal. The curve in black representing an incandescent blackbody radiator at various temperatures is shown on the chromaticity diagram. The color coordinates are defined for any light source that lies in the proximity of this curve or on the curve itself that can emit comfortable light for human eyesight.

An additional experiment was conducted to shed light on any symmetry distortion when Mn^{2+} is coordinated in the $K_2MnS_2H_4O_{10}$ crystal. For that, a $MnSO_4(H_2O)$ + deionized water solution, named $MnSH_2O_5$ + dw, was prepared, and its absorbance spectrum was measured. Figure 9 depicts a spectral comparison between the material in solution and the crystallized sample. Optical transitions to higher energy electronic states are only seen for crystal grown. Moreover, small shifts in position for the two lowest energy states are noticed (Fig. 9 inset). Therefore, these findings suggest that the Dq crystal field was slightly altered.

Usually, the crystal field splittings are represented on a Tanabe-Sugano (T–S) diagram. It describes multi-electron energy levels as a function of crystal field strength (Δ_0/B, $\Delta_0 = 10$ Dq) for a constant C/B, where B and C are the Racah parameters which indicate the magnitude of interelectronic repulsion between terms of same multiplicity [40].

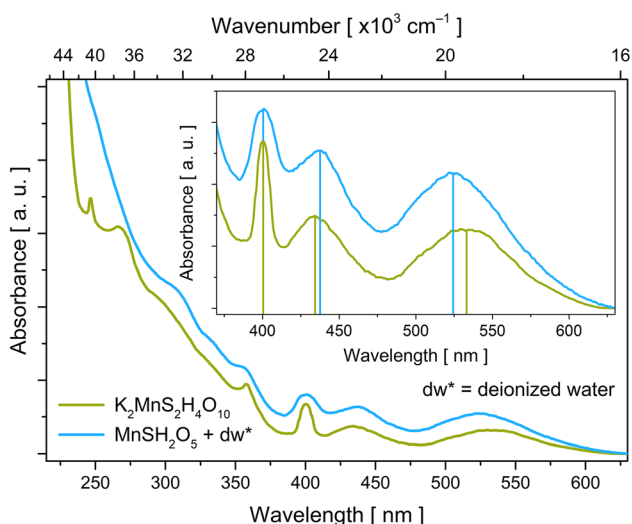According to UV–Vis optical absorbance spectrum of the crystal (Fig. 7a), the two lowest energy states are $v_1 = {}^6A_{1g}(S) \rightarrow {}^4T_{1g}(G) = 18{,}754.7$ cm^{-1}, and $v_2 = {}^6A_{1g}(S) \rightarrow {}^4T_{2g}(G) = 23{,}014.9$ cm^{-1}. The ratio between these energy bands is given by:

$$\frac{v_2}{v_1} = \frac{E_2/B}{E_1/B} = \frac{23014.9 \text{ cm}^{-1}}{18754.7 \text{ cm}^{-1}} \cong 1.227 \qquad (3)$$

By using the T–S diagram (Fig. S2), the ratio $(E_2/B)/(E_1/B)$ becomes $\cong 1.227$ when $\Delta_0/B = 12.51$. From Fig. S2, $E_1/B = 23.14$ and $E_2/B = 28.40$. In this approach, the Racah B parameter can be found calculating B from both v_1 and v_2, respectively: $B = (18{,}754.7$ cm$^{-1}/23.14) = 810.5$ cm^{-1}, and $B = (23{,}014.9$ cm$^{-1}/28.40) = 810.4$ cm^{-1}. Therefore, the average value of B is 810.4 cm^{-1}. The magnitude of ligand-field splitting was duly extracted by using the average value of the Racah B parameter: $\Delta_0/810.4$ cm$^{-1} = 12.51$, $\Delta_0 = 10{,}138.1$ cm^{-1}, and Dq $= 1013.8$ cm^{-1}.

The C parameter value was assessed from the experimental data using the expression for the energy (wavenumber) of the ${}^4E_g(G)$ electronic state [49]:

$$\text{Energy}\left[{}^6A_{1g}(S) \rightarrow {}^4 E_g(G)\right] = 10B + 5C \qquad (4)$$

Assuming the absorbance peak ≈ 400 nm to be the transition to the ${}^6A_{1g}(S) \rightarrow {}^4E_g(G)$ state, the following average value for the Racah C parameter was found: $C = 3374.2$ cm^{-1}. As a comparison, the values of the Racah parameters for the free Mn^{2+} ions are $B = 960$ cm^{-1} and $C = 3325.5$ cm^{-1}, with $C/B = 3.46$ [50]. For the Mn in $K_2MnS_2H_4O_{10}$ crystal, the ratio C/B is 4.16, and Dq$/B$ is 1.25. A ligand-field splitting interpretation suggests that the transition metal in the double salt crystal behaves as a relatively low-field ion since the H_2O molecule on the octahedron is a weak ligand.

The Racah parameters and the ligand-field splitting for the $MnSH_2O_5$ solubilized in deionized water are summarized in Table 4 (for calculations, see supplementary materials). The spectral line shape in the lowest energy region is remarkably similar to that reported by Jorgensen [51] for $MnSO_4$ in H_2O. For the Mn(II) sulfate monohydrate salt used here, a Dq$/B = 1.11$ was found.

Therefore, the spectroscopic data in Tables 3, 4 evidence that the host site of Mn, when in a double salt dihydrate, is indeed slightly distorted from regular octahedral or tetrahedral symmetry.

Figure 9 UV–Vis optical absorbance spectra of $K_2MnS_2H_4O_{10}$ single crystal and $MnSH_2O_5$ + deionized water solution.

Table 4 Data obtained from optical absorbance spectra and T-S diagram of Mn^{2+} ions into $K_2MnS_2H_4O_{10}$ single crystal and into $MnSH_2O_5$ solubilized in deionized water

Experimental parameters	Sample	
	$K_2MnS_2H_4O_{10}$	$MnSH_2O_5 + dw$
v_2/v_1	1.227	1.198
Δ_0/B	12.51	11.07
E_1/B	23.14	24.48
E_2/B	28.40	29.33
$< B >$ average	810.4 cm^{-1}	779.2 cm^{-1}
$< Dq >$ average	1013.8 cm^{-1}	862.6 cm^{-1}
C	3374.2 cm^{-1}	3374.2 cm^{-1}

Conclusions

Studies involving the structural, morphological, thermal, vibrational, and optical properties of kröhnkite-type $K_2MnS_2H_4O_{10}$ single crystals were presented and discussed. XRD pattern showed that the double salt crystallized in triclinic symmetry with $P\bar{1}$ (C_i^1) space group. Imperfections such as pores and cracks were observed on the crystal surface by SEM micrography. Electron diffraction of a selected area in an HRTEM image validated the triclinic atomic ordering. Thermal analyses indicated stability up to $\approx$ 360 K. Above this temperature, the crystal undergoes two phase transformations due to the liberation of two H_2O molecules of the crystal structure. Excellent agreement between theoretical (DFPT calculation) and experimental (FT-IR and Raman) vibration modes was noticed. An optical bandgap of 5.78 eV, typical of insulating materials, was estimated from the transmittance spectrum. UV–Vis absorbance spectrum revealed six characteristic ligand-field bands, consistent with sixfold coordinated Mn(II) complex. From the optical spectrum and Tanabe-Sugano diagram aid, the crystal-field strength and the Racah interelectronic-repulsion parameters were evaluated. Under 3.1 eV ($\approx$ 400 nm) excitation, a dual-emission due to the two different luminescent species was observed in the fluorescence spectrum; green–yellow ($\approx$ 562 nm) and orange ($\approx$ 598 nm— more emission intense). In this case, the emission spectrum comprises Mn^{2+} radiative centers in slightly distorted $[MnO_4(H_2O)_2]$ octahedral and $[MnO_4]$ tetrahedral sites. A fraction of Mn is supposedly tetrahedrally coordinated, corresponding to green–yellow emission. The results suggested that the $K_2Mn(SO_4)_2(H_2O)_2$ crystal is a promising material for several optical applications due to the cheap synthesis and the possibility of light emission tunability (from green to deep red) via changes in the Mn coordination number (four- and six-fold) and in the crystal-field strength by suitable doping or by the mixed crystal growing.

Declarations

Conflict of interest The authors declare that they have no known competing financial interests or personal relationships that could have appeared to influence the work reported in this paper.

Supplementary Information: The online version contains supplementary material available at https://doi.org/10.1007/s10853-022-07188-7.

References

[1] Barpanda P, Oyama G, Ling CD, Yamada A (2014) Krohnkite-type $Na_2Fe(SO_4)_2 \cdot 2H_2O$ as a novel 3.25 V insertion compound for Na-ion batteries. Chem Mater 26:1297–1299. https://doi.org/10.1021/cm4033226

[2] Marinova D, Kostov V, Nikolova R, Kukeva R, Zhecheva E, Sendova-Vasileva M, Stoyanova R (2015) From kröhnkite- to alluaudite-type of structure: novel method of synthesis of sodium manganese sulfates with electrochemical properties in alkali-metal ion batteries. J Mater Chem A 3:22287–22299. https://doi.org/10.1039/c5ta07204b

[3] Watcharatharapong T, Thienprasert J, Barpanda P, Ahuja R, Chakraborty S (2017) Mechanistic study of Na-ion diffusion and small polaron formation in kröhnkite $Na_2Fe(SO_4)_2 \cdot 2H_2O$ based cathode materials. J Mater Chem A 5:21726–21739. https://doi.org/10.1039/c7ta04508e

[4] Watcharatharapong T, T-Thienprasert J, Chakraborty S, Ahuja R (2019) Defect formations and pH-dependent kinetics in kröhnkite $Na_2Fe(SO_4)_2 \cdot 2H_2O$ based cathode for sodium-ion batteries: resembling synthesis conditions through chemical potential landscape. Nano Energy 55:123–134. https://doi.org/10.1016/j.nanoen.2018.10.038

[5] Ait Ousaleh H, Sair S, Zaki A, Faik A, Mirena Igartua J, El Bouari A (2020) Double hydrates salt as sustainable thermochemical energy storage materials: evaluation of dehydration behavior and structural phase transition reversibility. Sol Energy 201:846–856. https://doi.org/10.1016/j.solener.2020.03.067

[6] Fleck M, Kolitsch U, Hertweck B (2002) Natural and synthetic compounds with kröhnkite-type chains: review and classification. Zeitschrift Fur Krist 217:435–443. https://doi.org/10.1524/zkri.217.9.435.22883

[7] Fleck M, Kolitsch U, Hertweck B, Giester G, Wildner M, Prem M, Wohlschläger A (2002) Crystal structures of the double salt dihydrates $K_2Cd(SeO_4)_2 \cdot 2H_2O$, $K_2Mn(SO_4)_2 \cdot 2H_2O$, $(NH_4)_2Cu(SeO_4)_2 \cdot 2H_2O$ and $KFeH(SO_4)_2 \cdot 2H_2O$. Zeitschrift Fur Krist 217:242–248. https://doi.org/10.1524/zkri.217.6.242.22812

[8] Fleck M, Kolitsch U (2003) Natural and synthetic compounds with kröhnkite-type chains. An update, Zeitschrift Fur Krist 218:553–567. https://doi.org/10.1524/zkri.218.8.553.20689

[9] Kolitsch U, Fleck M (2005) Second update on compounds with kröhnkite-type chainsT. Z Kristallogr 220:31–41. https://doi.org/10.1524/zkri.220.1.31.58894

[10] Kolitsch U, Fleck M (2006) Third update on compounds with kröhnkite-type chains: the crystal structure of wendwilsonite $[Ca_2Mg(AsO_4)_2 \cdot 2H_2O]$ and the new triclinic structure types of synthetic $AgSc(CrO_4)_2 \cdot 2H_2O$ and $M_2Cu(Cr_2O_7)_2 \cdot 2H_2O$ (M = Rb, Cs). Eur J Mineral 18:471–482. https://doi.org/10.1127/0935-1221/2006/0018-0471

[11] Stoilova D, Georgiev M, Lengauer CL, Wildner M, Marinova D (2009) Vibrational behavior of SO_4^{2-} guest ions included in $K_2Me(CrO_4)_2 \cdot 2H_2O$ (Me = Co, Ni) and crystal structures of $K_2Me(CrO_4)_2 \cdot 2H_2O$ (Me = Co, Ni). J Mol Struct 920:289–296. https://doi.org/10.1016/j.molstruc.2008.11.013

[12] Frost RL, Yunfei X, Scholz R (2013) Vibrational spectroscopy of the copper (II) disodium sulphate dihydrate mineral kröhnkite $Na_2Cu(SO_4)_2 \cdot 2H_2O$. Spectrosc Lett 46:447–452. https://doi.org/10.1080/00387010.2012.753906

[13] Marinova DM, Zhecheva EN, Kukeva RR, Markov PV, Nihtianova DD, Stoyanova RK (2017) Mixed sodium nickel-manganese sulfates: crystal structure relationships between hydrates and anhydrous salts. J Solid State Chem 250:49–59. https://doi.org/10.1016/j.jssc.2017.03.015

[14] Marinova D, Wildner M, Bancheva T, Stoyanova R, Georgiev M, Stoilova DG (2018) Synthesis structure and properties of blödite-type solid solutions, $Na_2Co_{1-x}Cu_x(SO_4)_2 \cdot 4H_2O$ ($0<x \leq 0.18$), and crystal structure of synthetic kröhnkite, $Na_2Cu(SO_4)_2 \cdot 2H_2O$. Phys Chem Miner 45:801–817. https://doi.org/10.1007/s00269-018-0963-0

[15] Majzlan J, Marinova D, Dachs E (2021) Thermodynamics of the double sulfates $Na2M2+(SO4)2 \cdot nH2O$ (M = Mg, Mn Co, Ni, Cu, Zn, n = 2 or 4) of the blödite-kröhnkite family. RSC Adv 11:374–379. https://doi.org/10.1039/d0ra09501j

[16] Weil M, Kolitsch U (2021) $(NH_4)Mg(HSO_4)(SO_4)(H_2O)_2$ and $NaSc(CrO_4)2(H_2O)_2$, two crystal structures comprising kröhnkite-type chains, and the temperature-induced phase transition $(NH_4)Mg(HSO_4)(SO_4)(H_2O)_2 \leftrightarrow (NH_4)MgH(SO_4)_2(H_2O)_2$. Acta Cryst 77:144–151. https://doi.org/10.1107/S2053229621001650

[17] De A, Mondal N, Samanta A (2017) Luminescence tuning and exciton dynamics of Mn-doped $CsPbCl_3$ nanocrystals. Nanoscale 9:16722–16727. https://doi.org/10.1039/C7NR06745C

[18] Nandha NK, Nag A (2018) Synthesis and luminescence of Mn-doped $Cs_2AgInCl_6$ double perovskites. Chem Commun 54:5205–5208. https://doi.org/10.1039/C8CC01982G (**Camb**)

[19] Sun Q, Wang S, Zhao C, Leng J, Tian W, Jin S (2019) Excitation-dependent emission color tuning from an individual Mn-doped perovskite microcrystal. J Am Chem Soc 141:20089–20096. https://doi.org/10.1021/jacs.9b09143

[20] Li C, Bai X, Guo Y, Zou B (2019) Tunable emission properties of manganese chloride small single crystals by pyridine incorporation. ACS Omega 4:8039–8045. https://doi.org/10.1021/acsomega.8b03661

[21] Wei JH, Liao JF, Wang XD, Zhou L, Jiang Y, Bin Kuang D (2020) All-inorganic lead-free heterometallic $Cs_4MnBi_2Cl_{12}$ perovskite single crystal with highly efficient orange emission. Matter 3:892–903. https://doi.org/10.1016/j.matt.2020.05.018

[22] Rietveld HM (1967) Line profiles of neutron powder-diffraction peaks for structure refinement. Acta Crystallogr 22:151–152. https://doi.org/10.1107/S0365110X67000234

[23] Larson AC, Von Dreele RB (2004) General Structure Analysis System (GSAS), Los Alamos National Laboratory Report No. LAUR 86–748 https://11bm.xray.aps.anl.gov/documents/GSASManual.pdf

[24] Toby BH (2001) EXPGUI, a graphical user interface for GSAS. J Appl Crystallogr 34:210–213. https://doi.org/10.1107/S0021889801002242

[25] Ganz E, Pauli HKA (1995) Whiteness and tint formulas of the commission internationale de l'eclairage: approximations in the L*a*b* color space. Appl Opt 34:2998–2999. https://doi.org/10.1364/ao.34.002998

[26] Rajagopal AK, Callaway J (1973) Inhomogeneous electron gas. Phys Rev B 7:174111. https://doi.org/10.1103/PhysRevB.7.1912

[27] Kohn W, Sham LJ (1965) Self-consistent equations including exchange and correlation effects. Phys Rev 140:A1133–A1138. https://doi.org/10.1103/PhysRev.140.A1133

[28] Giannozzi P, Baroni S, Bonini N, Calandra M, Car R, Cavazzoni C, Ceresoli D, Chiarotti GL, Cococcioni M, Dabo I, Dal Corso A, de Gironcoli S, Fabris S, Fratesi G, Gebauer R, Gerstmann U, Gougoussis C, Kokalj A, Lazzeri M, Martin-Samos L, Marzari N, Mauri F, Mazzarello R, Paolini S, Pasquarello A, Paulatto L, Sbraccia C, Scandolo S, Sclauzero G, Seitsonen AP, Smogunov A, Umari P, Wentzcovitch RM (2009) QUANTUM ESPRESSO: a modular and open-source software project for quantum simulations of materials. J Phys Condens Matter 21:446–452. https://doi.org/10.1088/0953-8984/21/39/395502

[29] Baroni S, De Gironcoli S, Dal Corso A, Giannozzi P (2001) Phonons and related crystal properties from density-functional perturbation theory. Rev Mod Phys 73:515–562. https://doi.org/10.1103/RevModPhys.73.515

[30] Perdew JP, Zunger A (1981) Self-interaction correction to density-functional approximations for many-electron systems. Phys Rev B 23:5048–5079. https://doi.org/10.1103/PhysRevB.23.5048

[31] Monkhorst HJ, Pack JD (1976) Special points for Brillouin-zone integrations. Phys Rev B 13:5188–5192. https://doi.org/10.1103/PhysRevB.13.5188

[32] Grimme S (2006) Semiempirical GGA-type density functional constructed with a long-range dispersion correction. J Comput Chem 27:1787–1799. https://doi.org/10.1002/jcc.20495

[33] Urabe K, Shirakami T, Iwashima M (2004) Superstructure in a triclinic phase of TRICALCIUM silicate. J Am Ceram Soc 83:1253–1258. https://doi.org/10.1111/j.1151-2916.2000.tb01363.x

[34] Souamti A, Martín IR, Zayani L, Hernández-Rodríguez MA, Soler-Carracedo K, Lozano-Gorrín AD, Lalla E, Chehimi DBH (2016) Synthesis, characterization and spectroscopic properties of a new Nd3+-doped Co-picromerite-type tutton salt. J Lumin 177:93–98. https://doi.org/10.1016/j.jlumin.2016.04.033

[35] Arno H (2002) Reidies, "manganese compounds" in ullmann's encyclopedia of industrial chemistry. Wiley-VCH, Weinheim

[36] Ghosh S, Ullah S, de Mendonça JPA, Moura LG, Menezes MG, Flôres LS, Pacheco TS, de Oliveira LFC, Sato F, Ferreira SO (2019) Electronic properties and vibrational spectra of $(NH_4)_2M''(SO_4)_2 \cdot 6H_2O$ (M = Ni, Cu) Tutton's salt: DFT and experimental study. spectrochim acta - Part A mol Biomol Spectrosc 218:281–292. https://doi.org/10.1016/j.saa.2019.04.023

[37] Rao SVJ, Sreedhar AS, Rao B, Lakshman JL (1992) Electron paramagnetic resonance and optical absorption spectra of Mn^{2+} ions in alkali zinc borosulphate glasses. J Non Cryst Solids 144:169–174

[38] Tanabe Y, Sugano S (1954) On the absorption spectra of complex ions II. J Chem Soc Jpn 9:766–779

[39] Figgis BN, Hitchman MA (2000) Ligand field theory and Its applications. Wiley-VCH, New York

[40] Kamimura H, Sugano S, Tanabe Y (1970) Multiplets of transition-metal ions in crystals. Academic Press, New York

[41] Oka R, Kusukami K, Masui T (2020) Effect of $[MnO_6]$ octahedra to the coloring mechanism of $(Li_{1-x}Na_x)_2MnO_3$. ACS Omega 5(22):13108–13114. https://doi.org/10.1021/acsomega.0c01071

[42] Zhang D, Wang C, Liu Y, Shi Q, Wang W, Zhai Y (2012) Green and red photoluminescence from $ZnAl_2O_4$: Mn phosphors prepared by solgel method. J Lumin 132:1529–1531. https://doi.org/10.1016/j.jlumin.2012.01.025

[43] Molla AR, Chakradhar RPS, Kesavulu CR, Rao JL, Biswas SK (2012) EPR and optical properties of lithium disilicate glasses and glass-ceramics doped with Mn^{2+} ions. J Alloys Compd 512:105–114. https://doi.org/10.1016/j.jallcom.2011.09.031

[44] Choudhury B, Choudhury A (2013) Tailoring luminescence properties of TiO_2 nanoparticles by Mn doping. J Lumin 136:339–346. https://doi.org/10.1016/j.jlumin.2012.12.011

[45] Morad V, Cherniukh I, Pöttschacher L, Shynkarenko Y, Yakunin S, Kovalenko MV (2019) Manganese(II) in tetrahedral halide environment: factors governing bright green luminescence. Chem Mater 31(24):10161–10169. https://doi.org/10.1021/acs.chemmater.9b03782

[46] Zhou Q, Dolgov L, Srivastava AM, Zhou L, Wang Z, Shi J, Dramićanin MD, Brik MG, Wu M (2018) Mn^{2+} and Mn^{4+} red phosphors: synthesis, luminescence and applications in WLEDs. A review. J Mater Chem C 6:2652–2671. https://doi.org/10.1039/c8tc00251g

[47] Qin Y, She P, Huang X, Huang W, Zhao Q (2020) Luminescent manganese (II) complexes: synthesis, properties and

optoelectronic applications. Coord Chem Rev 416:213331. https://doi.org/10.1016/j.ccr.2020.213331

[48] McCamy CS (1992) Correlated color temperature as an explicit function of chromaticity coordinates. Color Res Appl 17:142–144. https://doi.org/10.1002/col.5080170211

[49] Griffith JS (1961) The theory of transition metal ions. Cambridge University press, Cambridge

[50] Uylings PHM, Raasen AJJ, Wyart JF (1984) Energies of N equivalent electrons expressed in terms of two-electron energies and independent three-electron parameters: a new complete set of orthogonal operators .II. Application to 3dN

configurations. J Phys B: At Mol Phys 17:4103–4126. https://doi.org/10.1088/0022-3700/17/20/010

[51] Jorgensen CH (1954) Studies of absorption spectra IV: some new transition group bands of low intensity. Acta Chem Scand 8(9):1502–1512. https://doi.org/10.3891/acta.chem.scand.08-1502